Heliyon 10 (2024) e24072

Contents lists available at ScienceDirect

Heliyon

journal homepage: www.cell.com/heliyon

Research article

# A quantum mechanical approach to the oxidation mechanism of graphene oxide (GO)

Dimitrios K. Papayannis [a,**], Konstantinos D. Papavasileiou [b,c,d], Vasilios S. Melissas [e,*]

[a] Department of Material Science and Engineering, University of Ioannina, GR–451 10, Ioannina, Greece
[b] Department of ChemoInformatics, NovaMechanics Ltd., CY-1070, Nicosia, Cyprus
[c] Division of Data Driven Innovation, Entelos Institute, CY-6059, Larnaca, Cyprus
[d] Department of ChemoInformatics, NovaMechanics MIKE., GR-185 45, Piraeus, Greece
[e] Department of Chemistry, University of Ioannina, GR–451 10, Ioannina, Greece

ARTICLE INFO

*Keywords:*
Graphene oxide cluster
Oxidation
ONIOM method
Ozonide
Ozone
1,3-Dioxetane
Exergonic reaction

ABSTRACT

Elucidation of the reaction mechanism concerning the oxidation above the face and at the edge of a large, oxidized graphene (GO) cluster, namely $C_{80}H_{22}O$, by molecular oxygen in the first excited state ($^1\Delta_g$) was achieved with quantum mechanical calculations using the ONIOM two-layer method. Oxidation on the face of the aforementioned cluster leads to the formation of an ozone molecule, whereas oxygen molecule attack at the edge of the oxidized graphene surface either launches an ozonide —a five-membered ring species— formation during its outward approach or an 1,3-dioxetane —a four-membered ring species— production along its inward invasion. A detailed examination of the proposed pathways suggests that the ozonide formation should overcome almost one and a half times an adiabatic energy barrier with respect to the ozone production and is strongly exergonic by up to −50.1 kcal mol$^{-1}$, supporting the experimental findings that both compounds are critically involved in the explosive deoxygenation of GO. On the other hand, the 1,3-dioxetane alternative pathway is considered even more exergonic, although it requires an overwhelming adiabatic energy barrier of 29.8 kcal mol$^{-1}$ to accomplish its target.

## 1. Introduction

Carbon is undoubtedly one of the most significant elements in the periodic table due to its unique ability to form strong covalent bonds with other carbon atoms or heteroatoms, which in turn leads to a myriad of stable configurations and structures. In recent decades, the classical allotropes of carbon (diamond and graphite) were enriched with the discovery of entirely new carbon allotropes, such as fullerenes [1,2], carbon nanotubes [3], mesoporous carbons like Carbon Mesostructured by KAIST (Korea Advanced Institute of Science and Technology) Number 3 (CMK-3) [4], graphene [5], and graphene oxide (GO) [6]. The latter two have attracted significant attention due to their extraordinary properties [7] and their potential application in various technological fields.

* Corresponding author.
** Corresponding author.
*E-mail addresses:* dpapagia@uoi.gr (D.K. Papayannis), papavasileiou@novamechanics.com (K.D. Papavasileiou), melissas@uoi.gr (V.S. Melissas).

https://doi.org/10.1016/j.heliyon.2024.e24072
Received 29 August 2023; Received in revised form 20 December 2023; Accepted 3 January 2024
Available online 6 January 2024

GO was first synthesized in 1859 by Brodie [8], and various mechanisms have been proposed to elucidate its structure and synthesis since then [9–13]. However, it took researchers almost 150 years to grasp its importance [14]. Initially, GO was used as a starting material for graphene production [15] and more recently as a material with unique properties of its own [6], which have rendered it a valuable material in various applications [16,17]. For example, Hernández Rosas et al. have investigated the electronic and chemical properties of graphene, graphane, and graphene oxide and observed that graphene and graphane structures exhibit semiconductor behavior, while graphene oxide exhibits semi-metallic behavior; removing the carboxyl group from graphene oxide is predicted to induce a transition from semi-metallic to semiconductor behavior [18]. GO-based materials hold significant potential in biomedical applications as versatile nanocarriers, drug and gene delivery vehicles, phototherapy, bioimaging, biosensing, tissue engineering, antibacterial agents, sensors, membranes, photovoltaics, green catalysis etc. [19–25].

Attention has also been given to GO for its ability to produce deoxygenated single graphene sheets under thermal expansion ("thermal-shock") [26]. GO is known to comprise a high number of oxygen-containing groups, and the number and type of those groups drastically affect the resulting exfoliated products during its thermal reduction [2,27–31]. Moreover, GO is highly energetic, thermally unstable and can readily undergo exothermic disproportionation reactions to produce chemically modified graphene under mild heating conditions [32]. To this end, the investigation of GO interactions with reactive oxygen species, such as molecular oxygen, has been the subject of several studies in order to understand its exposure to the environment [33,34]. In a published article by Qiu et al. [35], a detailed thermochemical and kinetic study of GO exothermic decomposition is presented, depicting spectroscopic and modeling evidence that epoxide groups are primarily responsible for the energetic behavior. This means that large samples of GO in certain storage and handling scenarios will be capable of self-heating and spontaneously decomposing, leading to high-volume gas release and explosive events. Although the explosive deoxygenation of GO has already been reported by Brodie [8] and was investigated further recently [35–38], a theoretical investigation of the possible mechanistic and energetic pathways of this explosive deoxygenation has not been reported to date. Therefore, it becomes clear that further work is mandatory to unravel mechanisms and kinetics involved in the explosive reduction process and fully characterize hazards associated with large-scale GO processing, while allow for its safe development and commercialization.

In this study, we performed theoretical calculations using the ONIOM two-layer method, ONIOM2 [39–44], to elucidate the GO oxidation mechanism. Experimental observations [35] fully corroborate our results, which allow the oxidation of a GO analogue to proceed through epoxide groups' molecular oxygen attack. As mentioned previously, experimental evidence indicates that epoxides elevate GO's formation energy, driving exothermic decomposition, while oxidized carbons displaying exothermic decomposition employ oxygen ring-generating oxidants such as ozone and permanganate to produce reactive ozonides [35]. In support of this, our computations show that initiation of the oxidation/deoxygenation process advances via two main possible highly exothermic pathways leading to the formation of ozone and ozonide/1,3-dioxetane, respectively, whereas both routes are characterized by moderate to large energy barriers. Specifically, we predict the oxidation of internal epoxide groups through a modest adiabatic energy barrier (17.92 kcal $mol^{-1}$) leading to an exergonic formation of ozone equal to −19.04 kcal $mol^{-1}$. As far as the edge epoxide groups are concerned, their interaction with molecular oxygen proceeds through a considerable adiabatic energy barrier equal to 26.44 kcal

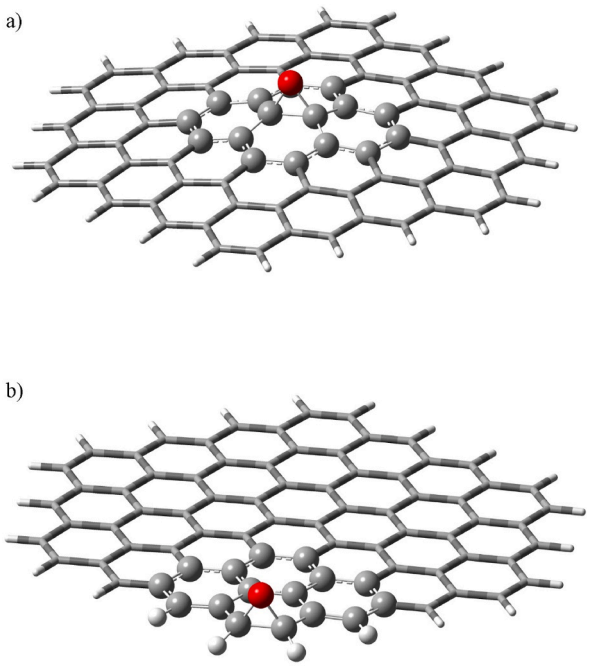


**Fig. 1.** Calculated model geometries of the graphene-oxide cluster ($C_{80}H_{22}O$) a) at the face and b) at the edge, respectively, at the ONIOM2: HSEH1PBE/cc-pVDZ//HF/3-21g level of theory.

mol$^{-1}$, leading afterward to ozonide formation with concomitant free energy release exceeding −50 kcal mol$^{-1}$. The proposed mechanism is likely to occur by contributing to the intense burning of the oxidized graphene basal plane, while justifying available experimental results.

## 2. Computational methods

A model graphene-like nanosheet was constructed by 30 fused benzene rings arranged in a single atomic layer containing 80 carbon atoms, with the edges saturated by hydrogen atoms, corresponding to the molecular formula $C_{80}H_{22}$. It was then treated quantum mechanically as a graphene-oxide cluster, $C_{80}H_{22}O$, employing the ONIOM (our own N-layered Integrated molecular Orbital and Molecular mechanics) method [45–47]. ONIOM is a versatile, robust and constantly evolving method with wide applicability in the computational study of chemical problems [48–50]. Accordingly, the four central carbon rings and the epoxide-like group are computationally treated at a high level of accuracy by implementing density functional theory (DFT) [51], whereas the rest of the system is taken into account at the Hartree-Fock (HF) level of theory [52] to further reduce the required computational time and resources, and to adequately represent the surrounding system (Fig. 1). The total energy of the system can be expressed, within the framework of the ONIOM2 methodology (i.e. two layers) developed by Vreven and Morokuma [53], as:

$$E_{ONIOM2} = E^{high}_{model} + E^{low}_{real} - E^{low}_{model}, \quad (1)$$

where *real* denotes the entire system, treated at the *low* level, and *model* denotes the part of the system of which the energy is calculated at both the *high* and *low* levels of theory (eq. (1)). As is always the case, the size of the *model* domain and that of the overall system (*real*) under study, plus the *low* level of theory implementation of the whole domain versus the *high* one, and, finally, the type of interaction between the two layers (mechanical versus electrostatic embedding) result in a compromise between accuracy and computational efficiency.

Representation of the *high* level of theory was achieved by the hybrid full Heyd-Scuseria-Ernzerhof functional (HSEH1PBE) [54–60], an excellent selection for quantitatively studying structure-function relations and the effects of chemical substitutions in graphene and its derivatives [61,62], in conjunction with Dunning's cc-pVDZ basis set [63,64]. The surrounding graphene environment was included by using the less expensive Hartree-Fock (HF) method [65–68] coupled with Pople's 3–21g basis set [69–71]. All calculations were carried out by means of the Gaussian 09 Quantum Chemistry Package (Revision D.01) [72]. All geometries were calculated with a tight criterion geometry optimization. Vibrational frequencies were calculated at the same levels of theory to further identify and validate the nature of the stationary points (0 negative eigenvalues of their analytic Hessian matrix for minima and 1 for transition states), while additional intrinsic reaction coordinate (IRC) calculations were performed to properly indicate corresponding reactants and products for each transition state. The vibrational modes and the corresponding frequencies are based on a harmonic approximation (HO), which was accomplished for all calculated structures at the HSEH1PBE/cc-pVDZ//HF/3-21g level of theory. Zero-point energies (ZPE) were included to correct calculated energetics for all modes, resulting in the vibrationally adiabatic potential energy value, $V^G_a$, for each stationary point. Finally, inclusion of enthalpic and entropic corrections at 298 K leads to free energy values for each available point, allowing for a proper consideration of the activation energy for each participating elementary reaction.

The second point is the proper consideration of the singlet-triplet molecular oxygen energy gap ($^1\Delta_g$)$O_2$-($^3\Sigma^-_g$)$O_2$. This value is experimentally established to be 22.5 kcal mol$^{-1}$, although several *ab initio* and DFT methodologies, for example CCSD(T) and B3LYP calculations, yield an energy splitting of ($^1\Delta_g$) $O_2$-($^3\Sigma^-_g$) $O_2$ close to 30 kcal mol$^{-1}$ [73–80]. Multireference methods, for example CASPT2 [74–81], or use of complex type orbitals [75,76] lead to a proper description of ($^1\Delta_g$) $O_2$ and a correct description of the singlet potential energy surface (PES).

For the calculation of the excited electronic state of $O_2$, we employed the approach described in the work of Decharin et al. [82]. Specifically, the $O_2$ excited state was calculated as the single-point energy using spin-unrestricted DFT at the triplet-optimized $O_2$ structure. The electronic configuration of the converged SCF wavefunctions was confirmed by the $<S^2>$ values. The spin-contaminated open-shell singlet total energy is corrected by using a spin-projection method reported by Yamaguchi et al. [83]. This treatment yields a singlet-triplet energy difference of 20.5 kcal mol$^{-1}$ for molecular oxygen according to the scheme:

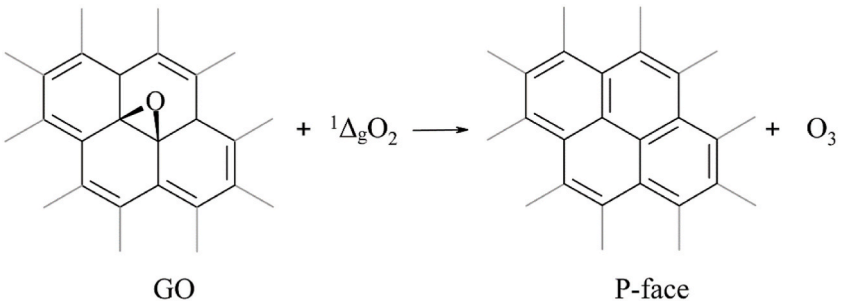


**Scheme 1.** Proposed reaction mechanism leading to the oxidation/deoxygenation above the face (face mechanism) of the $C_{80}H_{22}O$ cluster (GO) by singlet ($^1\Delta_g$) molecular oxygen ($O_2$) resulting in $C_{80}H_{22}$ and ozone ($O_3$) at the ONIOM2: HSEH1PBE/cc-pVDZ//HF/3-21g level of theory.

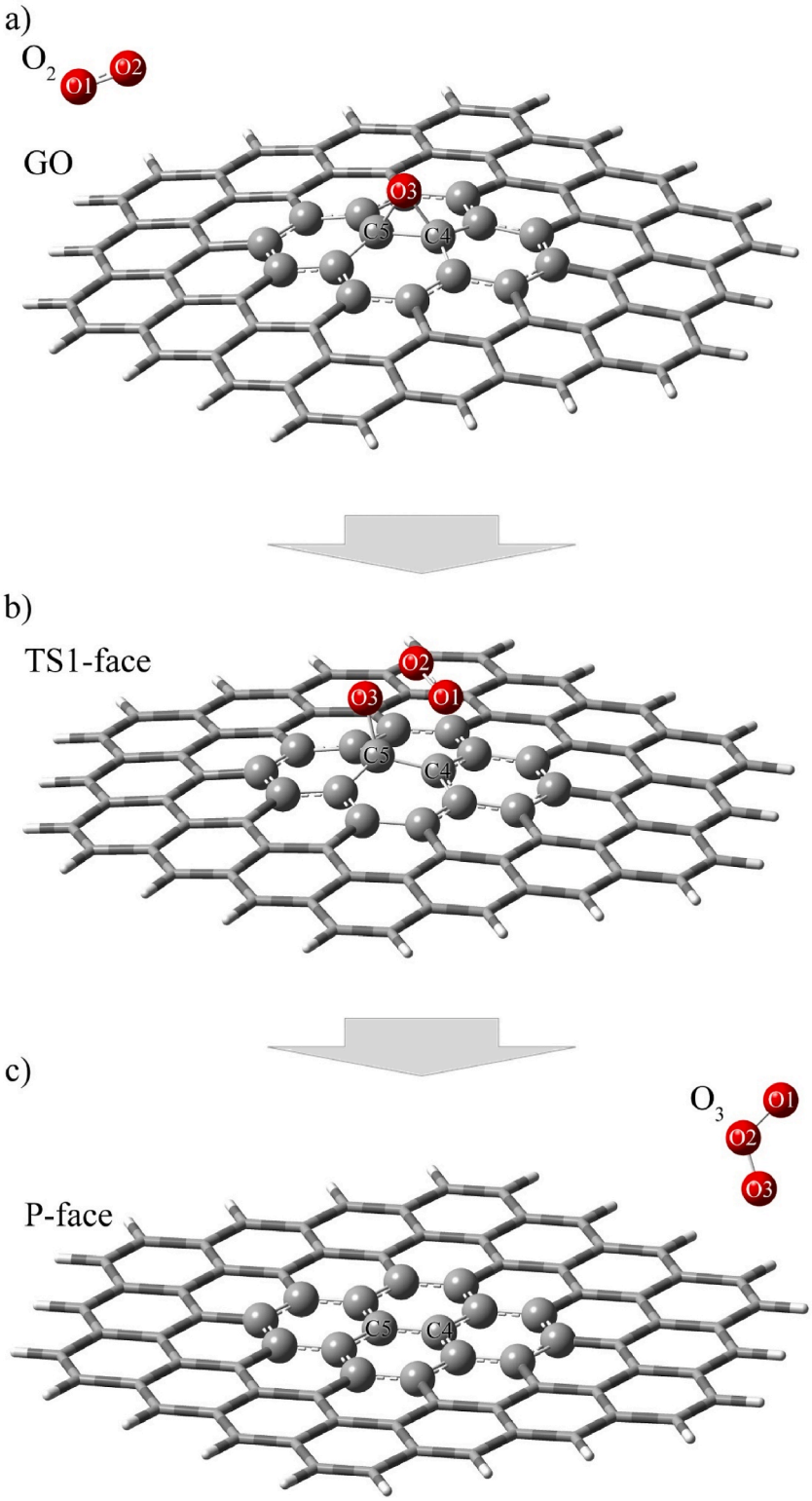


**Fig. 2.** Oxidation/deoxygenation reaction mechanism above the face (face mechanism) of the a) $C_{80}H_{22}O$ graphene oxidized cluster (GO) by singlet ($^1\Delta_g$) molecular oxygen ($O_2$) via the b) TS1-face transition state formation leads to the c) $C_{80}H_{22}$ graphene cluster (P-face) and ozone ($O_3$) evolution at the ONIOM2: HSEH1PBE/cc-pVDZ//HF/3-21g level of theory.

$$^{1}E_{\text{spin-corrected-DFT}} = {}^{1}E_{UDFT} + \frac{^{1}\langle S^2\rangle}{^{3}\langle S^2\rangle - {}^{1}\langle S^2\rangle}\left[{}^{1}E_{UDFT} - {}^{3}E_{UDFT}\right], \quad (2)$$

where $^{1}E_{spin-corrected-DFT}$ is the spin-corrected energy of the closed-shell singlet and, $^{1}E_{UDFT}$ and $^{3}E_{UDFT}$ denote the closed-shell singlet and the open-shell triplet energies, respectively (eq. (2)).

## 3. Theoretical study of oxidation/reduction-deoxygenation of GO

### 3.1. Molecular geometry

A detailed investigation of the reaction mechanisms leading to the oxidation/deoxygenation above the face (face mechanism) (Scheme 1, Fig. 2) and at the edge (edge mechanism) (Scheme 2, Figs. 3 and 4) of a large graphene oxidized cluster ($C_{80}H_{22}O$) by singlet ($^{1}\Delta_g$) molecular oxygen is presented. Singlet oxygen, an excited form of molecular oxygen, is considered a milder choice of an oxidizing agent not expected to cause permanent damage, e.g. rapture of the carbon cluster, when added to the graphene oxide surface [84]. Meanwhile, the ($^{1}\Delta_g$) $O_2$ is expected to react smoothly with GO leading exothermically to the respective product [85,86]. All calculated structures are also provided as *xyz* files.

The face mechanism exothermically leads to reduction of GO and ozone, $O_3$, formation via a four-membered transition state (abbr. TS1-face) structure (Fig. 2). Initially, as the singlet $O_2$ molecule (O1–O2) approaches an oxygen atom (O3) lying on the GO surface, the atomic oxygen entity is simultaneously engaged in terminating one of its surface bonds (O3–C4) and creating a new one (O3–O2) with the invading $O_2$ molecule, as a precursor to ozone's formation. The TS1-face transition state species remarkably illuminates this process, while allowing ozone's emergence and restoration of graphene surface's planarity (abbr. P-face). TS1-face geometry is characterized by an O1–O2 distance equal to 1.224 Å, an O2–O3 distance of 1.797 Å, an O1–O2–O3 angle equal to 111.040°, an O2–O3–C5 angle equal to 112.049° and an O1–O2–O3–C5 almost planar dihedral angle equal to 13.237° (Fig. S1).

Participation of the dual edge mechanism includes initial attack of a singlet $O_2$ molecule at the edge of the oxidized graphene surface, which either launches an ozonide—a five-membered ring species—formation during its outward approach (Fig. 3) or an 1,3-dioxetane—a four-membered ring species—evolution along its inward invasion (Fig. 4).

Along the outward approach of the excited $O_2$ molecule (O1–O2) at the edge of the oxidized graphene surface, the diatom exhibits its preference to land on top of the plane while simultaneously bonds its nearest oxygen atom (O1) with two terminal carbon atoms (C3–C4) already bearing an oxygen atom (O5) on the bottom planar side (Fig. 3). The other molecular oxygen atom (O2) remains intact facing the outward side of the reaction field. Oxidation proceeds through the TS1-outward edge transition state elucidation, where the

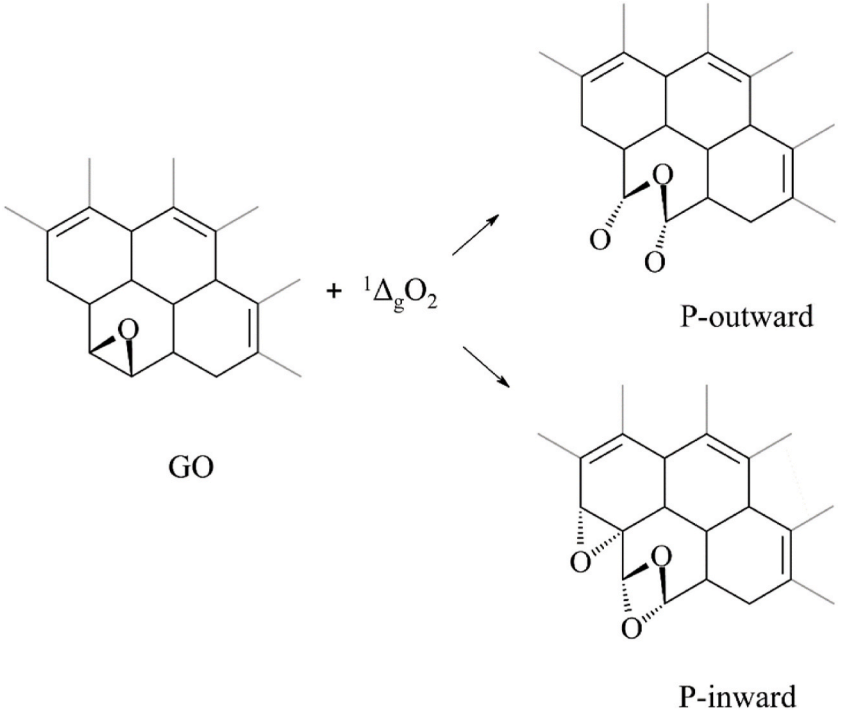


**Scheme 2.** Proposed reaction mechanism leading to the oxidation/deoxygenation at the edge (edge mechanism-outward approach) of the $C_{80}H_{22}O$ cluster (GO) by singlet ($^{1}\Delta_g$) molecular oxygen ($O_2$) at the ONIOM2: HSEH1PBE/cc-pVDZ//HF/3-21g level of theory, resulting in ozonide and 1,3-dioxetane formation along its outward and inward approach, respectively.

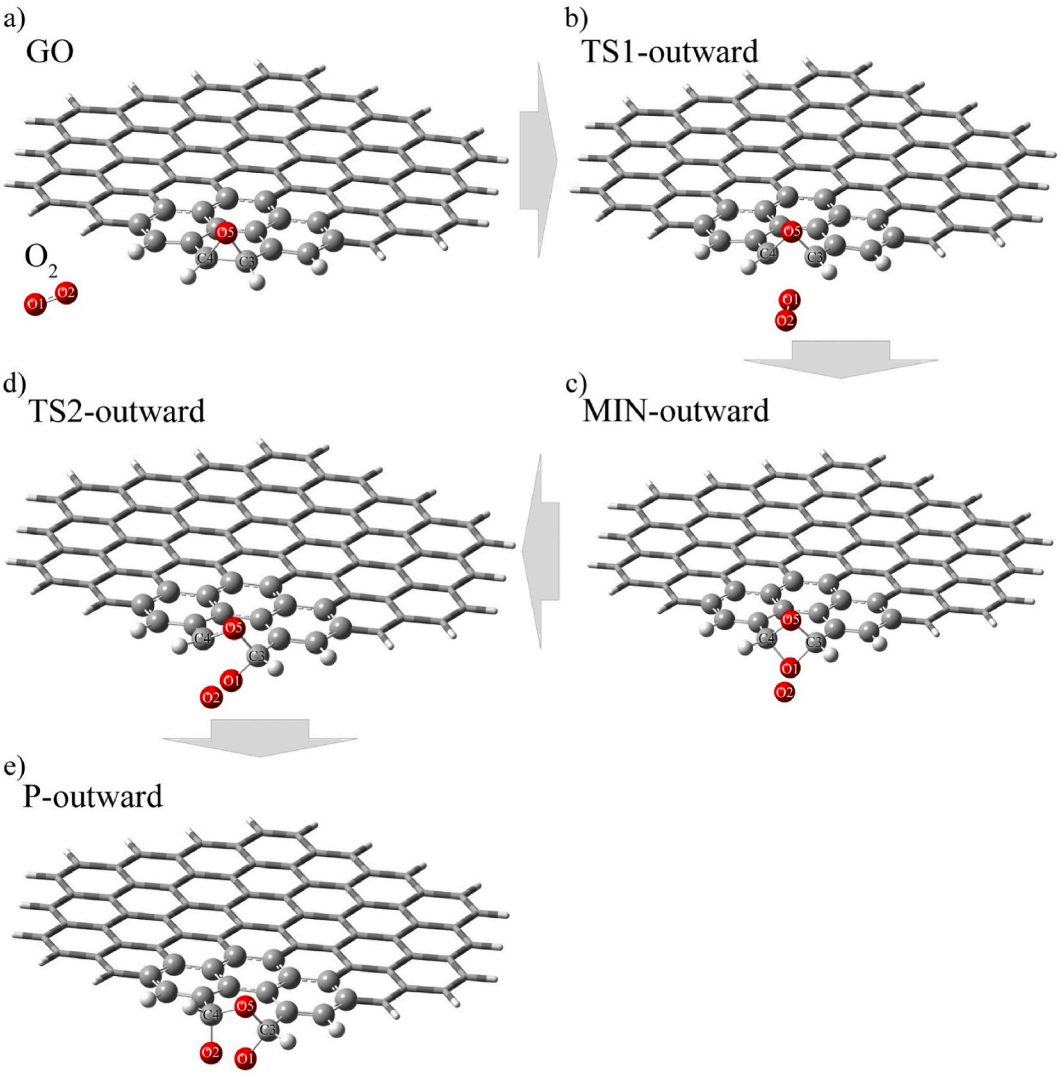


**Fig. 3.** Outward oxidation/deoxygenation reaction mechanism at the edge (edge mechanism-outward approach) of the a) $C_{80}H_{22}O$ graphene oxidized cluster (GO) by singlet ($^1\Delta_g$) molecular oxygen ($O_2$) proceeds outwardly via the b) TS1-outward formation to the c) MIN-outward intermediate evolution, which further advances to the d) TS2-outward introduction and, finally, to the e) ozonide (P-outward) release at the ONIOM2: HSEH1PBE/cc-pVDZ//HF/3-21g level of theory.

O1 atom adopts an equidistant position from C3 and C4 equal to 1.966 Å and allows for the formation of an equilateral triangle with the two carbon atoms. The O1–O2 distance elongates to 1.262 Å while the C3–O1–C4 angle embraces a value equal to 54.616° and the C3–O5–C4 one advances 18° with respect to its initial GO value (Fig. S2). As a result, a similar minimum-outward (abbr. MIN-outward) intermediate structure emerges, where the O1–O2 distance further extends to 1.447 Å, the C3–O1–C4 angle escalates to 82.360° and the C3–O5–C4 one amplifies to 88.739°. The O5 atom retains an equidistant position from C3 and C4 equal to 1.394 Å at the TS1-outward structure, which slightly elongates to 1.407 Å at the minimum-outward equilibrium point. Both terminal carbon atoms (C3 and C4) discard their mutual bonding upon the TS1-outward edge transition state formation and until the ozonide evolution (Fig. S3). Since the minimum-outward intermediate arrival, the so far nonparticipating in the reaction O2 atom initiates its encounter in the terrain as it approaches the C4 terminal atom and simultaneously departs from its O1 partner. The whole rearrangement leads to the TS2-outward edge transition state emergence, an ozonide's precursor, where the O1–O2 bond stretches to 1.502 Å, the O1–C3 distance reduces to 1.406 Å and the O2 atom advances towards the C4 one (Fig. S4). The O5–C3 bond lengthens to 1.443 Å and the O5–C4 one shrinks to 1.342 Å. In addition, the O1–C3–O5 angle adopts a 100.300° value and the O2–C4–O5 one turns equal to 89.691°, whereas the C3–O1–O2–C4 dihedral angle emerges to 73.209° (Fig. S4). Finally, the reaction scheme leads to the ozonide formation (abbr. P-outward), a five membered ring species which sequentially comprises O1–O2–C4–O5–C3 atoms, attached almost vertically to the GO plane via the two carbon atoms. Therefore, the O1–O2 bond dwindles to 1.433 Å, the O1–C3 one extends to 1.439 Å while the O2–C4 shrinks to 1.407 Å, and the O5–C3 distance reduces to 1.402 Å whilst the O5–C4 increases to 1.391 Å. Both the

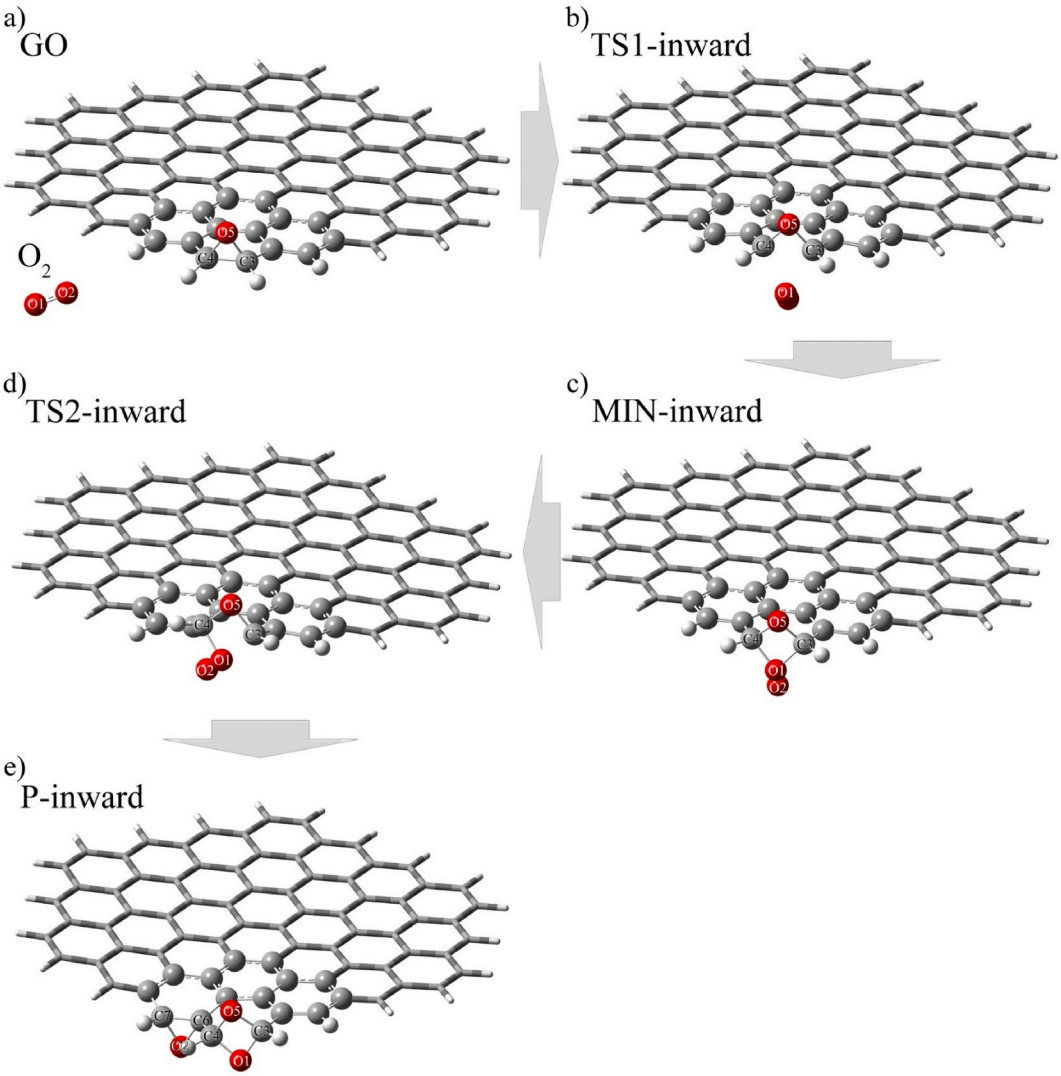


**Fig. 4.** Inward oxidation/deoxygenation reaction mechanism at the edge (edge mechanism-inward invasion) of the a) $C_{80}H_{22}O$ graphene oxidized cluster (GO) by singlet ($^1\Delta_g$) molecular oxygen ($O_2$) proceeds inwardly via the b) TS1-inward development to the c) MIN-inward intermediate evolution, which further advances to the d) TS2-inward formation and, finally, to the e) 1,3-dioxetane (P-inward) appearance at the ONIOM2: HSEH1PBE/cc-pVDZ//HF/3-21g level of theory.

O1–C3–O5 and the O2–C4–O5 angles rise to 106.598° and 103.611°, respectively, although the C3–O1–O2–C4 dihedral angle diminishes to 35.751° (Fig. S5).

Similarly, the inward alternative collision of $^1\Delta_g$ $O_2$ (O1–O2) molecules with terminal carbon atoms (C3–C4) of the GO surface occurs on top of the reaction plane (Fig. 4). In detail, the closest molecular oxygen atom (O1) approaches in between the selected carbon atoms (C3–C4), which already carry an oxygen atom (O5) on the other planar side, while the other molecular oxygen atom (O2) faces towards the inward side of the GO plane. Subsequently, the TS1-inward edge transition state evolves, where the O1 and O5 atoms are positioned 2.010 Å and 1.391 Å equidistantly from the C3 and C4 atoms, respectively, and mirror plane with respect to the GO level, both adopting equilateral geometries where the arising C3–O1–C4 angle equals 54.802° and the C3–O5–C4 one elongates to 83.374° (Fig. S6). It is worthwhile to mention the C3–C4 bond cleavage upon the transition state unveiling and until the dioxetane formation. The O1–C3–O5–C4 dihedral angle deduces a −14.359° value, resembling a rhomboid shape, whereas the O1–O2 distance extends to 1.256 Å (Fig. S6). Afterward, the minimum-inward intermediate develops (abbr. MIN-inward), while retaining similar structural characteristics to the TS1-inward edge stationary point. Major geometrical differences to its predecessor include further extension of the O1–O2 bond to 1.404 Å, the C3–O1–C4 angle rise to 82.870° and the C3–O5–C4 one widening to 90.563°, shrinkage of the O1–C3/C4 bonds to 1.511 Å and stretching of the O5–C3/C4 ones to 1.407 Å, and further reduction of the O1–C3–O5–C4 dihedral angle to −20.073° (Fig. S7). Next reaction step consists of the TS2-inward edge transition state evolution, 1,3-dioxetane's precursor, where the O2 atom initiates its transfer on top of the adjacent terminal carbon ring and among C6 and C7 atoms. O1–C3 bond elongates

**Table 1**

Calculated reaction energetics (in kcal mol$^{-1}$) for the forward ($\Delta V_{MEP}^{\ddagger,for}$, $\Delta V_{G,for}^{a,\ddagger}$ and $\Delta G_{for}^{o,\ddagger}$) and backward ($\Delta V_{MEP}^{\ddagger,back}$, $\Delta V_{G,back}^{a,\ddagger}$ and $\Delta G_{back}^{o,\ddagger}$) associated barriers of the face mechanism, leading to the reduction of GO and $O_3$ formation along the minimum energy path, at the ONIOM2: HSEH1PBE/cc-pVDZ//HF/3-21G level of theory. The overall zero of energy for the forward and backward barriers is set at the reactants and products level, respectively.

| Face mechanism | | | | | | |
|---|---|---|---|---|---|---|
| | $\Delta V_{MEP}^{rxn}$ | | $\Delta V_{G}^{a,rxn}$ | | $\Delta G_{rxn}^{0}$ | |
| GO + $O_2$ → P-face + $O_3$ | −18.31 | | −16.78 | | −19.04 | |
| | $\Delta V_{MEP}^{\ddagger,for}$ | $\Delta V_{MEP}^{\ddagger,back}$ | $\Delta V_{G,for}^{a,\ddagger}$ | $\Delta V_{G,back}^{a,\ddagger}$ | $\Delta G_{for}^{o,\ddagger}$ | $\Delta G_{back}^{o,\ddagger}$ |
| GO + $O_2$ → P-face + $O_3$ | 17.24 | 35.55 | 17.92 | 34.70 | 27.48 | 46.52 |

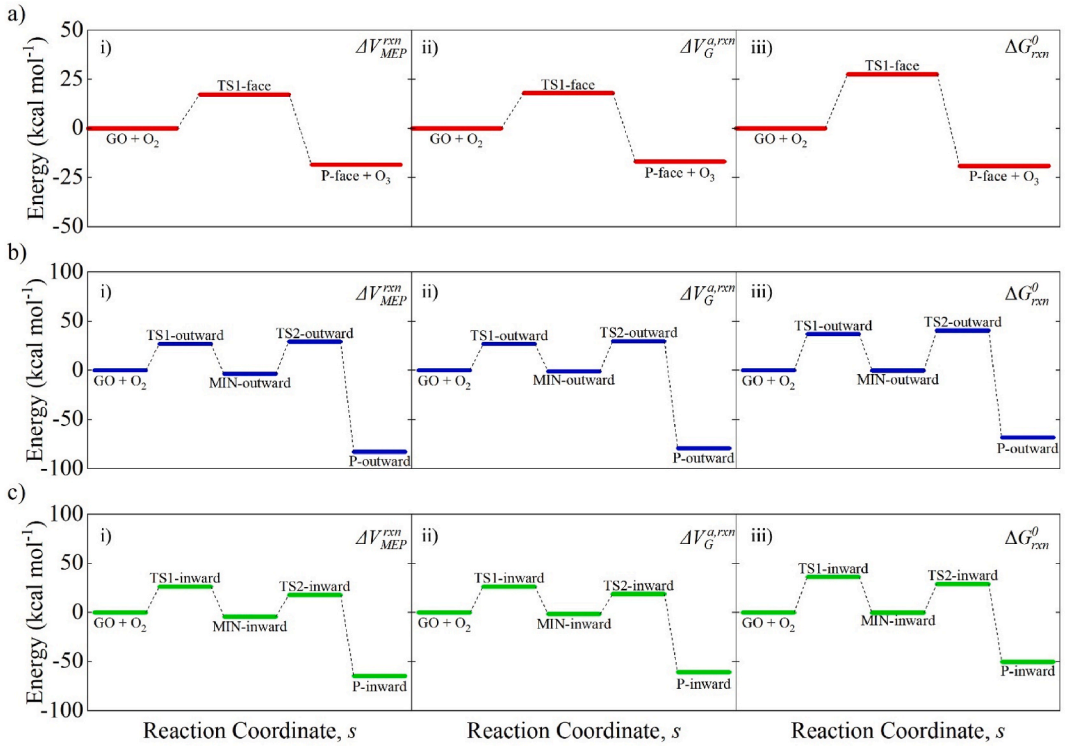


**Fig. 5.** Calculated i) relative Born-Oppenheimer (classical), $V_{MEP}$, ii) adiabatic ground-state (classical ones with zero-point energy correction), $V_G^a$, and iii) free energy, $G^o$, profiles of the $C_{80}H_{22}O$ graphene oxide cluster (GO) oxidation/deoxyganation mechanisms by singlet ($^1\Delta_g$) molecular oxygen ($O_2$) a) above the face (red), namely GO + $O_2$ → TS1-face → P-face + $O_3$, b) at the edge site through the outward approach (blue), specifically GO + $O_2$ → TS1-outward → MIN-outward → TS2-outward → P-outward, and c) at the edge site throughout the inward invasion (green), precisely GO + $O_2$ → TS1-inward → MIN-inward → TS2-inward → P-inward, along the reaction coordinate, *s*, and at the ONIOM2: HSEH1PBE/cc-pVDZ//HF/3-21g level of theory. Reactants, GO + $O_2$, are always considered as the reference state.

to 1.538 Å whereas the O1–C4 one shrinks to 1.481 Å, and similarly the O5–C3 extends to 1.417 Å while the O5–C4 dwindles to 1.392 Å (Fig. S8). Both C3–O1–C4 and C3–O5–C4 angles adopt values almost equal to their TS2-inward counterparts, whilst the O1–C3–O5–C4 dihedral angle slightly reduces to −17.652° (Fig. S8). The inward edge reaction path concludes with the 1,3-dioxetane arrival (abbr. P-inward) and the O2 bounce on top of the GO plane and amongst the C6–C7 bond. The O1–C3 and O1–C4 bonds shrink to 1.426 Å and 1.416 Å, respectively, although the O5–C3 and O5–C4 ones spread to 1.428 Å and 1.416 Å, correspondingly. The C3–O1–C4 angle adopts a value of 85.040° and the C3–O5–C4 one shrinks to 84.972°. Accordingly, the O2–C6 and O2–C7 bonds slightly elongate by less than 0.01 Å and the C6–O2–C7 angle assumes a 62.280° value. The O1–C3–O5–C4 dihedral angle further diminishes to −14.715° establishing a vertical position for 1,3-dioxetane with respect to the GO plane (Fig. S9).

### *3.2. Reaction energetics*

Energies reported in this article are relative Born-Oppenheimer (classical) ones, $V_{MEP}$, adiabatic ground-state (classical ones with zero-point energy correction) ones, $V_G^a$, and free energy ones, $G^o$. All calculated energetics and vibrational frequencies characterizing

**Table 2**

Calculated reaction energetics (in kcal mol$^{-1}$) for the forward ($\Delta V^{\ddagger,for}_{MEP}$, $\Delta V^{a,\ddagger}_{G,for}$ and $\Delta G^{o,\ddagger}_{for}$) and backward ($\Delta V^{\ddagger,back}_{MEP}$, $\Delta V^{a,\ddagger}_{G,back}$ and $\Delta G^{o,\ddagger}_{back}$) associated barriers of the edge mechanism, leading to the production of ozonide ($P_{outw}$) and 1,3-dioxetane ($P_{inw}$) along the outward (outw) and inward (inw) minimum energy paths, respectively, at the ONIOM2: HSEH1PBE/cc-pVDZ//HF/3-21G level of theory. The overall zero of energy for the forward and backward barriers is always set at the reactants and products level, respectively.

| Edge mechanism-Outward reaction | | | | | | |
|---|---|---|---|---|---|---|
| | $\Delta V^{rxn}_{MEP}$ | | $\Delta V^{a,rxn}_{G}$ | | $\Delta G^{0}_{rxn}$ | |
| GO + $O_2$ → MIN-outward | −4.01 | | −1.45 | | 8.92 | |
| MIN-outward → P-outward | −60.25 | | −58.98 | | −58.98 | |
| GO + $O_2$ → P-outward | −64.26 | | −60.43 | | −50.06 | |
| | $\Delta V^{\ddagger,for}_{MEP}$ | $\Delta V^{\ddagger,back}_{MEP}$ | $\Delta V^{a,\ddagger}_{G,for}$ | $\Delta V^{a,\ddagger}_{G,back}$ | $\Delta G^{o,\ddagger}_{for}$ | $\Delta G^{o,\ddagger}_{back}$ |
| GO + $O_2$ → MIN-outward | 26.36 | 30.37 | 26.44 | 27.89 | 36.27 | 27.35 |
| MIN-outward → P-outward | 21.77 | 82.02 | 20.18 | 79.16 | 20.11 | 79.09 |
| GO + $O_2$ → P-outward | 26.36 | 90.62 | 26.44 | 86.87 | 36.27 | 86.33 |
| Edge mechanism-Inward reaction | | | | | | |
| | $\Delta V^{rxn}_{MEP}$ | | $\Delta V^{a,rxn}_{G}$ | | $\Delta G^{0}_{rxn}$ | |
| GO + $O_2$ → MIN-inward | −3.36 | | −1.04 | | 9.29 | |
| MIN-inward → P-inward | −79.30 | | −77.90 | | −77.45 | |
| GO + $O_2$ → P-inward | −82.66 | | −78.94 | | −68.16 | |
| | $\Delta V^{\ddagger,for}_{MEP}$ | $\Delta V^{\ddagger,back}_{MEP}$ | $\Delta V^{a,\ddagger}_{G,for}$ | $\Delta V^{a,\ddagger}_{G,back}$ | $\Delta G^{o,\ddagger}_{for}$ | $\Delta G^{o,\ddagger}_{back}$ |
| GO + $O_2$ → MIN-inward | 27.16 | 30.52 | 26.98 | 28.02 | 36.99 | 27.70 |
| MIN-inward → P-inward | 32.70 | 112.00 | 30.84 | 108.73 | 31.46 | 108.91 |
| GO + $O_2$ → P-inward | 29.34 | 109.82 | 29.80 | 105.92 | 40.75 | 105.15 |

each stationary point on the calculated minimum energy path (MEP) are reported in Tables S1 and S2.

In detail, Table 1 reports all considered reaction energetics, namely $\Delta V^{rxn}_{MEP}$, $\Delta V^{a,rxn}_{G}$ and $\Delta G^{o}_{rxn}$ for the aforementioned face mechanism leading to reduction of GO and $O_3$ formation along the minimum energy path, and the corresponding forward ($\Delta V^{\ddagger,for}_{MEP}$, $\Delta V^{a,\ddagger}_{G,for}$ and $\Delta G^{o,\ddagger}_{for}$) and backward ($\Delta V^{\ddagger,back}_{MEP}$, $\Delta V^{a,\ddagger}_{G,back}$ and $\Delta G^{o,\ddagger}_{back}$) barrier heights.

Seemingly, the face mechanism exhibits an 17.92 kcal mol$^{-1}$ adiabatic forward barrier height and an 34.70 kcal mol$^{-1}$ adiabatic backward one, which proclaims reaction's $\Delta V^{a,rxn}_{G}$ equal to −16.78 kcal mol$^{-1}$ (Fig. 5a). Consideration of free energy aspects results to an exergonic reaction of −19.04 kcal mol$^{-1}$ and an 27.48 kcal mol$^{-1}$ free energy forward barrier height (Fig. 5a), undoubtedly leading to a reactant-like transition state structure in agreement with Hammond's postulate [87].

On the other hand, in Table 2 the reaction energetics for the dual edge mechanism initiation via intermediates emergence prior to ozonide's formation and 1,3-dioxetane's evolution are presented. Both mechanisms proceed via an intermediate minimum structure formation, namely the MIN-outward and MIN-inward intermediates, exhibiting adiabatic forward barrier heights equal to 26.44 kcal mol$^{-1}$ (adopting the TS1-outward edge transition state structure) and 26.98 kcal mol$^{-1}$ (embracing the TS1-inward edge transition state conformation), respectively (Table 2, Fig. 5b and c). Regarding their adiabatic backward barrier heights, the outward reaction assumes an 27.89 kcal mol$^{-1}$ value and the minimum-inward formation equals to 28.02 kcal mol$^{-1}$, presumably leading to comparable respective $\Delta V^{a,rxn}_{G}$ values of −1.45 kcal mol$^{-1}$ and -1.04 kcal mol$^{-1}$ (Fig. 5). However, the free energy forward barrier height values for the MIN-outward production equals 36.27 kcal mol$^{-1}$ and for the MIN-inward development escalates to 36.99 kcal mol$^{-1}$, characterizing both reactions as endergonic and assuming $\Delta G^{o}_{rxn}$ values of 8.92 kcal mol$^{-1}$ and 9.29 kcal mol$^{-1}$, respectively (Table 2, Fig. 5c).

The dual edge mechanism further progresses from the minimum-outward intermediate towards ozonide via an 20.18 kcal mol$^{-1}$ adiabatic forward barrier height, correspondingly the TS2-outward edge transition state structure, and a restrictive 79.16 kcal mol$^{-1}$ adiabatic backward one, leading to an $\Delta V^{a,rxn}_{G}$ value of −58.98 kcal mol$^{-1}$ (Fig. 5). Moreover, the minimum-inward intermediate advances to 1,3-dioxetane via a considerable 30.84 kcal mol$^{-1}$ adiabatic forward barrier height, namely the TS2-inward edge transition state conformation, and a prohibitive 108.74 kcal mol$^{-1}$ adiabatic backward one, prompting to a colossal $\Delta V^{a,rxn}_{G}$ equal to −77.90 kcal mol$^{-1}$. Finally, former reactions from the minimum-outward intermediate to ozonide and from the minimum-inward intermediate to 1,3-dioxetane bear free energy forward barrier height values equal to 20.11 kcal mol$^{-1}$ and 31.46 kcal mol$^{-1}$, respectively, assuming their exergonic $\Delta G^{o}_{rxn}$ values equal to −58.98 kcal mol$^{-1}$ for ozonide's production and −77.45 kcal mol$^{-1}$ regarding 1,3-dioxetane's formation (Table 2).

## 4. Conclusions

Oxidation, via molecular oxygen in the first excited state ($^1\Delta_g$), on the face of the $C_{80}H_{22}O$ cluster leads to $O_3$ formation, whereas $O_2$ ($^1\Delta_g$) attack at the edge of the $C_{80}H_{22}O$ surface either launches an ozonide formation during its outward approach or an 1,3-dioxetane production along its inward invasion. The face mechanism remains the main pathway of the GO oxidation process, finally leading to reduction of the GO and $O_3$ formation. It exhibits an 17.92 kcal mol$^{-1}$ adiabatic forward barrier height and an 27.48 kcal mol$^{-1}$ free energy one, while its exoergicity yield turns equal to −19.04 kcal mol$^{-1}$. However, the dual edge mechanism operates complementary

to the face one. In detail, its primary path proceeds through the minimum-outward intermediate towards ozonide via two consecutive forward barrier heights, where the dominant one applies to the TS1-outward energetics bearing an 26.44 kcal $mol^{-1}$ adiabatic value and an 36.27 kcal $mol^{-1}$ free energy one. Similarly, the secondary path propagates through the minimum-inward intermediate towards 1,3-dioxetane via two successive forward barrier heights. The prevailing adiabatic forward barrier height encounters the TS2-inward energetics carrying an 30.84 kcal $mol^{-1}$ value and the effective free energy one equals 36.99 kcal $mol^{-1}$ applying to the TS1-inward conformation. Finally, the primary path assumes an exergonic $\Delta G^{o}_{rxn}$ value equal to −50.06 kcal $mol^{-1}$, whereas the secondary one lowers to −68.16 kcal $mol^{-1}$.

## CRediT authorship contribution statement

**Dimitrios K. Papayannis:** Writing - review & editing, Writing - original draft, Visualization, Software, Methodology, Investigation, Conceptualization. **Konstantinos D. Papavasileiou:** Writing - review & editing, Writing - original draft, Visualization, Validation, Software, Methodology, Investigation. **Vasilios S. Melissas:** Writing - review & editing, Writing - original draft, Visualization, Validation, Supervision, Software, Resources, Project administration, Methodology, Investigation, Conceptualization.

## Declaration of competing interest

The authors declare that they have no known competing financial interests or personal relationships that could have appeared to influence the work reported in this paper.

## Appendix B. Supplementary data

Supplementary data to this article can be found online at https://doi.org/10.1016/j.heliyon.2024.e24072.

## References

[1] H.W. Kroto, J.R. Heath, S.C. O'Brien, R.F. Curl, R.E. Smalley, C60: buckminsterfullerene, Nature 318 (1985) 162–163, https://doi.org/10.1038/318162a0.
[2] M. Acik, G. Lee, C. Mattevi, M. Chhowalla, K. Cho, Y.J. Chabal, Unusual infrared-absorption mechanism in thermally reduced graphene oxide, Nat. Mater. 9 (2010) 840–845, https://doi.org/10.1038/nmat2858.
[3] S. Iijima, Helical microtubules of graphitic carbon, Nature 354 (1991) 56–58, https://doi.org/10.1038/354056a0.
[4] S. Jun, S.H. Joo, R. Ryoo, M. Kruk, M. Jaroniec, Z. Liu, T. Ohsuna, O. Terasaki, Synthesis of new, nanoporous carbon with hexagonally ordered mesostructure, J. Am. Chem. Soc. 122 (2000) 10712–10713, https://doi.org/10.1021/ja002261e.
[5] K.S. Novoselov, A.K. Geim, S.V. Morozov, D. Jiang, Y. Zhang, S.V. Dubonos, I.V. Grigorieva, A.A. Firsov, Electric field effect in atomically thin carbon films, Science 306 (2004) 666–669, https://doi.org/10.1126/science.1102896.
[6] D.R. Dreyer, S. Park, C.W. Bielawski, R.S. Ruoff, The chemistry of graphene oxide, Chem. Soc. Rev. 39 (2010) 228–240, https://doi.org/10.1039/B917103G.
[7] K.S. Novoselov, A.K. Geim, S.V. Morozov, D. Jiang, M.I. Katsnelson, I.V. Grigorieva, S.V. Dubonos, A.A. Firsov, Two-dimensional gas of massless Dirac fermions in graphene, Nature 438 (2005) 197–200, https://doi.org/10.1038/nature04233.
[8] B.C. Brodie, XIII. On the atomic weight of graphite, diPhilos. Trans. R. Soc. Lond. 149 (1859) 249–259, https://doi.org/10.1098/rstl.1859.0013.
[9] A.M. Dimiev, J.M. Tour, Mechanism of graphene oxide formation, ACS Nano 8 (2014) 3060–3068, https://doi.org/10.1021/nn500606a.
[10] A.M. Dimiev, Mechanism of Formation and Chemical Structure of Graphene Oxide, Graphene Oxide, 2016, pp. 36–84, https://doi.org/10.1002/9781119069447.ch2.
[11] L. Sun, Structure and synthesis of graphene oxide, Chin. J. Chem. Eng. 27 (2019) 2251–2260, https://doi.org/10.1016/j.cjche.2019.05.003.
[12] T. Nakajima, Y. Matsuo, Formation process and structure of graphite oxide, Carbon 32 (1994) 469–475, https://doi.org/10.1016/0008-6223(94)90168-6.
[13] H. Yang, G. Hanyu, Chemical synthesis of reduced graphene oxide: a review, Miner. Miner. Mater. 2 (2023) 8, https://doi.org/10.20517/mmm.2023.07.
[14] K. Raidongia, A.T.L. Tan, J. Huang, Chapter 14 - graphene oxide: some new insights into an old material, in: K. Tanaka, S. Iijima (Eds.), Carbon Nanotubes and Graphene, second ed., Elsevier, Oxford, 2014, pp. 341–374, https://doi.org/10.1016/B978-0-08-098232-8.00014-0.
[15] G. Shao, Y. Lu, F. Wu, C. Yang, F. Zeng, Q. Wu, Graphene oxide: the mechanisms of oxidation and exfoliation, J. Mater. Sci. 47 (2012) 4400–4409, https://doi.org/10.1007/s10853-012-6294-5.
[16] S.C. Ray, Chapter 2 - application and uses of graphene oxide and reduced graphene oxide, in: S.C. Ray (Ed.), Applications of Graphene and Graphene-Oxide Based Nanomaterials, William Andrew Publishing, Oxford, 2015, pp. 39–55, https://doi.org/10.1016/B978-0-323-37521-4.00002-9.
[17] J.L. Suter, P.V. Coveney, Principles governing control of aggregation and dispersion of aqueous graphene oxide, Sci. Rep. 11 (2021) 22460, https://doi.org/10.1038/s41598-021-01626-3.
[18] J.J. Hernandez Rosas, R.E. Ramirez Gutierrez, A. Escobedo-Morales, E. Chigo Anota, First principles calculations of the electronic and chemical properties of graphene, graphane, and graphene oxide, J. Mol. Model. 17 (2011) 1133–1139, https://doi.org/10.1007/s00894-010-0818-1.
[19] N. Bellier, P. Baipaywad, N. Ryu, J.Y. Lee, H. Park, Recent biomedical advancements in graphene oxide- and reduced graphene oxide-based nanocomposite nanocarriers, Biomater. Res. 26 (2022) 65, https://doi.org/10.1186/s40824-022-00313-2.
[20] S.J. Rowley-Neale, E.P. Randviir, A.S. Abo Dena, C.E. Banks, An overview of recent applications of reduced graphene oxide as a basis of electroanalytical sensing platforms, Appl. Mater. Today 10 (2018) 218–226, https://doi.org/10.1016/j.apmt.2017.11.010.
[21] R.K. Joshi, S. Alwarappan, M. Yoshimura, V. Sahajwalla, Y. Nishina, Graphene oxide: the new membrane material, Appl. Mater. Today 1 (2015) 1–12, https://doi.org/10.1016/j.apmt.2015.06.002.
[22] A. Singh, N. Sharma, M. Arif, R.S. Katiyar, Electrically reduced graphene oxide for photovoltaic application, J. Mater. Res. 34 (2019) 652–660, https://doi.org/10.1557/jmr.2019.32.
[23] H. Sachdeva, Recent advances in the catalytic applications of GO/rGO for green organic synthesis, Green Process. Synth. 9 (2020) 515–537, https://doi.org/10.1515/gps-2020-0055.
[24] F. Catania, E. Marras, M. Giorcelli, P. Jagdale, L. Lavagna, A. Tagliaferro, M. Bartoli, A review on recent advancements of graphene and graphene-related materials in biological applications, Appl. Sci. 11 (2021) 614.
[25] M.H.M. Facure, R. Schneider, A.D. Alvarenga, L.A. Mercante, D.S. Correa, Forms of Graphene I—Graphene Oxide and Reduced Graphene Oxide, Recent Advances in Graphene and Graphene-Based Technologies, IOP Publishing, 2023, https://doi.org/10.1088/978-0-7503-3999-5ch3, 3-1-3-27.

[26] M.J. McAllister, J.-L. Li, D.H. Adamson, H.C. Schniepp, A.A. Abdala, J. Liu, M. Herrera-Alonso, D.L. Milius, R. Car, R.K. Prud'homme, I.A. Aksay, Single sheet functionalized graphene by oxidation and thermal expansion of graphite, Chem. Mater. 19 (2007) 4396–4404, https://doi.org/10.1021/cm0630800.

[27] W. Gao, L.B. Alemany, L. Ci, P.M. Ajayan, New insights into the structure and reduction of graphite oxide, Nat. Chem. 1 (2009) 403–408, https://doi.org/10.1038/nchem.281.

[28] M. Acik, G. Lee, C. Mattevi, A. Pirkle, R.M. Wallace, M. Chhowalla, K. Cho, Y. Chabal, The role of oxygen during thermal reduction of graphene oxide studied by infrared absorption spectroscopy, J. Phys. Chem. C 115 (2011) 19761–19781, https://doi.org/10.1021/jp2052618.

[29] R. Larciprete, S. Fabris, T. Sun, P. Lacovig, A. Baraldi, S. Lizzit, Dual path mechanism in the thermal reduction of graphene oxide, J. Am. Chem. Soc. 133 (2011) 17315–17321, https://doi.org/10.1021/ja205168x.

[30] S. Kim, S. Zhou, Y. Hu, M. Acik, Y.J. Chabal, C. Berger, W. de Heer, A. Bongiorno, E. Riedo, Room-temperature metastability of multilayer graphene oxide films, Nat. Mater. 11 (2012) 544–549, https://doi.org/10.1038/nmat3316.

[31] Y. Zhu, X. Li, Q. Cai, Z. Sun, G. Casillas, M. Jose-Yacaman, R. Verduzco, J.M. Tour, Quantitative analysis of structure and bandgap changes in graphene oxide nanoribbons during thermal annealing, J. Am. Chem. Soc. 134 (2012) 11774–11780, https://doi.org/10.1021/ja304471x.

[32] D. Krishnan, F. Kim, J. Luo, R. Cruz-Silva, L.J. Cote, H.D. Jang, J. Huang, Energetic graphene oxide: challenges and opportunities, Nano Today 7 (2012) 137–152, https://doi.org/10.1016/j.nantod.2012.02.003.

[33] H.-S. Hsieh, R.G. Zepp, Reactivity of graphene oxide with reactive oxygen species (hydroxyl radical, singlet oxygen, and superoxide anion), Environ. Sci.: Nano 6 (2019) 3734–3744, https://doi.org/10.1039/C9EN00693A.

[34] C. Felip-León, M. Puche, J.F. Miravet, F. Galindo, M. Feliz, A spectroscopic study to assess the photogeneration of singlet oxygen by graphene oxide, Mater. Lett. 251 (2019) 45–51, https://doi.org/10.1016/j.matlet.2019.05.001.

[35] Y. Qiu, F. Collin, R.H. Hurt, I. Külaots, Thermochemistry and kinetics of graphite oxide exothermic decomposition for safety in large-scale storage and processing, Carbon 96 (2016) 20–28, https://doi.org/10.1016/j.carbon.2015.09.040.

[36] A.M. Rodríguez, P.V. Jiménez, Thermal decomposition of the graphite oxidation products, Thermochim. Acta 78 (1984) 113–122, https://doi.org/10.1016/0040-6031(84)87138-5.

[37] P.S.V. Jimenez, Thermal decomposition of graphite oxidation products DSC studies of internal combustion of graphite oxide, Mater. Res. Bull. 22 (1987) 601–608, https://doi.org/10.1016/0025-5408(87)90108-5.

[38] Y. Qiu, F. Guo, R. Hurt, I. Külaots, Explosive thermal reduction of graphene oxide-based materials: mechanism and safety implications, Carbon 72 (2014) 215–223, https://doi.org/10.1016/j.carbon.2014.02.005.

[39] F. Maseras, K. Morokuma, IMOMM: a new integrated ab initio + molecular mechanics geometry optimization scheme of equilibrium structures and transition states, J. Comput. Chem. 16 (1995) 1170–1179, https://doi.org/10.1002/jcc.540160911.

[40] S. Humbel, S. Sieber, K. Morokuma, The IMOMO method: integration of different levels of molecular orbital approximations for geometry optimization of large systems: test for n-butane conformation and $S_N2$ reaction: RCl+Cl$^-$, J. Chem. Phys. 105 (1996) 1959–1967, https://doi.org/10.1063/1.472065.

[41] T. Vreven, K.S. Byun, I. Komáromi, S. Dapprich, J.A. Montgomery, K. Morokuma, M.J. Frisch, Combining quantum mechanics methods with molecular mechanics methods in ONIOM, J. Chem. Theor. Comput. 2 (2006) 815–826, https://doi.org/10.1021/ct050289g.

[42] L.W. Chung, H. Hirao, X. Li, K. Morokuma, The ONIOM method: its foundation and applications to metalloenzymes and photobiology, WIREs Comput. Mol. Sci. 2 (2012) 327–350, https://doi.org/10.1002/wcms.85.

[43] T. Vreven, K. Morokuma, Prediction of the dissociation energy of hexaphenylethane using the ONIOM(MO:MO:MO) method, J. Phys. Chem. A 106 (2002) 6167–6170, https://doi.org/10.1021/jp014588n.

[44] K. Morokuma, Q. Wang, T. Vreven, Performance evaluation of the three-layer ONIOM method: case study for a zwitterionic peptide, J. Chem. Theor. Comput. 2 (2006) 1317–1324, https://doi.org/10.1021/ct600135b.

[45] S. Dapprich, I. Komáromi, K.S. Byun, K. Morokuma, M.J. Frisch, A new ONIOM implementation in Gaussian98. Part I. The calculation of energies, gradients, vibrational frequencies and electric field derivatives[1] Dedicated to Professor Keiji Morokuma in celebration of his 65$^{th}$ birthday, J. Mol. Struct. 461–462 (1999) 1–21, https://doi.org/10.1016/S0166-1280(98)00475-8.

[46] T. Vreven, K. Morokuma, Chapter 3 hybrid methods: ONIOM(QM:MM) and QM/MM, in: D.C. Spellmeyer (Ed.), Annual Reports in Computational Chemistry, Elsevier, 2006, pp. 35–51, https://doi.org/10.1016/S1574-1400(06)02003-2.

[47] M. Svensson, S. Humbel, R.D.J. Froese, T. Matsubara, S. Sieber, K. Morokuma, ONIOM: a multilayered integrated mo + MM method for geometry optimizations and single point energy predictions. A test for Diels−Alder reactions and Pt(P($t$-Bu)$_3$)$_2$ + H$_2$ oxidative addition, J. Phys. Chem. 100 (1996) 19357–19363, https://doi.org/10.1021/jp962071j.

[48] C. Plett, A. Katbashev, S. Ehlert, S. Grimme, M. Bursch, ONIOM meets xtb: efficient, accurate, and robust multi-layer simulations across the periodic table, Phys. Chem. Chem. Phys. 25 (2023) 17860–17868, https://doi.org/10.1039/d3cp02178e.

[49] P. Seeber, S. Seidenath, J. Steinmetzer, S. Gräfe, Growing Spicy ONIOMs: extending and generalizing concepts of ONIOM and many body expansions, WIREs Comput Mol Sci 13 (2023) e1644, https://doi.org/10.1002/wcms.1644.

[50] L.W. Chung, W.M.C. Sameera, R. Ramozzi, A.J. Page, M. Hatanaka, G.P. Petrova, T.V. Harris, X. Li, Z. Ke, F. Liu, H.-B. Li, L. Ding, K. Morokuma, The ONIOM method and its applications, Chem. Rev. 115 (2015) 5678–5796, https://doi.org/10.1021/cr5004419.

[51] W. Kohn, L.J. Sham, Self-Consistent equations including exchange and correlation effects, Phys. Rev. 140 (1965) A1133–A1138, https://doi.org/10.1103/PhysRev.140.A1133.

[52] W.J.R. Hehre, L, R. von, P. Schleyer, J. Pople, Ab Iinitio Molecular Orbital Theory, first ed. ed., Wiley-Interscience, 1986.

[53] T. Vreven, K. Morokuma, On the application of the IMOMO (integrated molecular orbital + molecular orbital) method, J. Comput. Chem. 21 (2000) 1419–1432, https://doi.org/10.1002/1096-987X(200012)21:16<1419::AID-JCC1>3.0.CO;2-C.

[54] J. Heyd, J.E. Peralta, G.E. Scuseria, R.L. Martin, Energy band gaps and lattice parameters evaluated with the Heyd-Scuseria-Ernzerhof screened hybrid functional, J. Chem. Phys. 123 (2005) 174101, https://doi.org/10.1063/1.2085170.

[55] J. Heyd, G.E. Scuseria, Efficient hybrid density functional calculations in solids: assessment of the Heyd–Scuseria–Ernzerhof screened Coulomb hybrid functional, J. Chem. Phys. 121 (2004) 1187–1192, https://doi.org/10.1063/1.1760074.

[56] J. Heyd, G.E. Scuseria, Assessment and validation of a screened Coulomb hybrid density functional, J. Chem. Phys. 120 (2004) 7274–7280, https://doi.org/10.1063/1.1668634.

[57] J. Heyd, G.E. Scuseria, M. Ernzerhof, Erratum: "Hybrid functionals based on a screened Coulomb potential", J. Chem. Phys. 124 (2006) 219906 https://doi.org/10.1063/1.2204597, 118, 8207 (2003)].

[58] A.F. Izmaylov, G.E. Scuseria, M.J. Frisch, Efficient evaluation of short-range Hartree-Fock exchange in large molecules and periodic systems, J. Chem. Phys. 125 (2006) 104103, https://doi.org/10.1063/1.2347713.

[59] A.V. Krukau, O.A. Vydrov, A.F. Izmaylov, G.E. Scuseria, Influence of the exchange screening parameter on the performance of screened hybrid functionals, J. Chem. Phys. 125 (2006) 224106, https://doi.org/10.1063/1.2404663.

[60] T.M. Henderson, A.F. Izmaylov, G. Scalmani, G.E. Scuseria, Can short-range hybrids describe long-range-dependent properties? J. Chem. Phys. 131 (2009) 044108 https://doi.org/10.1063/1.3185673.

[61] V. Barone, O. Hod, J.E. Peralta, G.E. Scuseria, Accurate prediction of the electronic properties of low-dimensional graphene derivatives using a screened hybrid density functional, Acc. Chem. Res. 44 (2011) 269–279, https://doi.org/10.1021/ar100137c.

[62] Y.-M. Liu, H. Hou, Y.-Z. Zhou, X.-J. Zhao, C. Tang, Y.-Z. Tan, K. Müllen, Nanographenes as electron-deficient cores of donor-acceptor systems, Nat. Commun. 9 (2018) 1901, https://doi.org/10.1038/s41467-018-04321-6.

[63] T.H.D. Jr, Gaussian basis sets for use in correlated molecular calculations. I. The atoms boron through neon and hydrogen, J. Chem. Phys. 90 (1989) 1007–1023, https://doi.org/10.1063/1.456153.

[64] E.R. Davidson, Comment on "Comment on Dunning's correlation-consistent basis sets", Chem. Phys. Lett. 260 (1996) 514–518, https://doi.org/10.1016/0009-2614(96)00917-7.

[65] C.C.J. Roothaan, New developments in molecular orbital theory, Rev. Mod. Phys. 23 (1951) 69–89, https://doi.org/10.1103/RevModPhys.23.69.
[66] G. Berthier, Extension de la méthode du champ moleculaire self-consistent a l'étude des états à couches incomplètes, C. R. Hebd. Seances Acad. Sci. 238 (1954) 91–93.
[67] J.A. Pople, R.K. Nesbet, Self-Consistent orbitals for radicals, J. Chem. Phys. 22 (1954) 571–572, https://doi.org/10.1063/1.1740120.
[68] R. McWeeny, G. Diercksen, Self-Consistent perturbation theory. II. Extension to open shells, J. Chem. Phys. 49 (1968) 4852–4856, https://doi.org/10.1063/1.1669970.
[69] J.S. Binkley, J.A. Pople, W.J. Hehre, Self-consistent molecular orbital methods. 21. Small split-valence basis sets for first-row elements, J. Am. Chem. Soc. 102 (1980) 939–947, https://doi.org/10.1021/ja00523a008.
[70] M.S. Gordon, J.S. Binkley, J.A. Pople, W.J. Pietro, W.J. Hehre, Self-consistent molecular-orbital methods. 22. Small split-valence basis sets for second-row elements, J. Am. Chem. Soc. 104 (1982) 2797–2803, https://doi.org/10.1021/ja00374a017.
[71] W.J. Pietro, M.M. Francl, W.J. Hehre, D.J. DeFrees, J.A. Pople, J.S. Binkley, Self-consistent molecular orbital methods. 24. Supplemented small split-valence basis sets for second-row elements, J. Am. Chem. Soc. 104 (1982) 5039–5048, https://doi.org/10.1021/ja00383a007.
[72] G.W.T.M.J. Frisch, H.B. Schlegel, G.E. Scuseria, M.A. Robb, J.R. Cheeseman, G. Scalmani, V. Barone, B. Mennucci, G.A. Petersson, H. Nakatsuji, M. Caricato, X. Li, H.P. Hratchian, A.F. Izmaylov, J. Bloino, G. Zheng, J.L. Sonnenberg, M. Hada, M. Ehara, K. Toyota, R. Fukuda, J. Hasegawa, M. Ishida, T. Nakajima, Y. Honda, O. Kitao, H. Nakai, T. Vreven, J.A. Montgomery Jr., J.E. Peralta, F. Ogliaro, M. Bearpark, J.J. Heyd, E. Brothers, K.N. Kudin, V.N. Staroverov, R. Kobayashi, J. Normand, K. Raghavachari, A. Rendell, J.C. Burant, S.S. Iyengar, J. Tomasi, M. Cossi, N. Rega, J.M. Millam, M. Klene, J.E. Knox, J.B. Cross, V. Bakken, C. Adamo, J. Jaramillo, R. Gomperts, R.E. Stratmann, O. Yazyev, A.J. Austin, R. Cammi, C. Pomelli, J.W. Ochterski, R.L. Martin, K. Morokuma, V. G. Zakrzewski, G.A. Voth, P. Salvador, J.J. Dannenberg, S. Dapprich, A.D. Daniels, Ö. Farkas, J.B. Foresman, J.V. Ortiz, J. Cioslowski, D.J. Fox, Gaussian09, Gaussian Inc., Wallingford CT, 2013.
[73] C. Hontoria-Lucas, A.J. López-Peinado, J.d.D. López-González, M.L. Rojas-Cervantes, R.M. Martín-Aranda, Study of oxygen-containing groups in a series of graphite oxides: physical and chemical characterization, Carbon 33 (1995) 1585–1592, https://doi.org/10.1016/0008-6223(95)00120-3.
[74] H.A. Becerril, J. Mao, Z. Liu, R.M. Stoltenberg, Z. Bao, Y. Chen, Evaluation of solution-processed reduced graphene oxide films as transparent conductors, ACS Nano 2 (2008) 463–470, https://doi.org/10.1021/nn700375n.
[75] P. Bazuła, A.-H. Lu, J.-J. Nitz, F. Schüth, Surface and pore structure modification of ordered mesoporous carbons via a chemical oxidation approach, Microporous Mesoporous Mater. 108 (2008) 266–275, https://doi.org/10.1016/j.micromeso.2007.04.008.
[76] F. Cataldo, G. Compagnini, L. D'Urso, G. Palleschi, F. Valentini, G. Angelini, T. Braun, Characterization of graphene nanoribbons from the unzipping of MWCNTs, Fullerenes, Nanotub. Carbon Nanostruct. 18 (2010) 261–272, https://doi.org/10.1080/15363831003782981.
[77] C.K. Kohlmiller, L. Andrews, Infrared spectrum of the primary ozonide of ethylene in solid xenon, J. Am. Chem. Soc. 103 (1981) 2578–2583, https://doi.org/10.1021/ja00400a016.
[78] J. Oxley, J. Smith, J. Brady, F. Dubnikova, R. Kosloff, L. Zeiri, Y. Zeiri, Raman and infrared fingerprint spectroscopy of peroxide-based explosives, J. Appl. Spectrosc. 62 (2008) 906–915, https://doi.org/10.1366/000370208785284420.
[79] V. Vacque, B. Sombret, J.P. Huvenne, P. Legrand, S. Suc, Characterisation of the O-O peroxide bond by vibrational spectroscopy, Spectrochim. Acta 53 (1997) 55–66, https://doi.org/10.1016/S1386-1425(97)83009-0.
[80] M.J. Lázaro, L. Calvillo, E.G. Bordejé, R. Moliner, R. Juan, C.R. Ruiz, Functionalization of ordered mesoporous carbons synthesized with SBA-15 silica as template, Microporous Mesoporous Mater. 103 (2007) 158–165, https://doi.org/10.1016/j.micromeso.2007.01.047.
[81] A. Stein, Z. Wang, M.A. Fierke, Functionalization of porous carbon materials with designed pore architecture, Adv. Mater. 21 (2009) 265–293, https://doi.org/10.1002/adma.200801492.
[82] N. Decharin, B.V. Popp, S.S. Stahl, Reaction of $O_2$ with [(−)-Sparteine]Pd(H)Cl: evidence for an intramolecular $[H–L]^+$ "reductive elimination" pathway, J. Am. Chem. Soc. 133 (2011) 13268–13271, https://doi.org/10.1021/ja204989p.
[83] K. Yamaguchi, F. Jensen, A. Dorigo, K.N. Houk, A spin correction procedure for unrestricted Hartree-Fock and Møller-Plesset wavefunctions for singlet diradicals and polyradicals, Chem. Phys. Lett. 149 (1988) 537–542, https://doi.org/10.1016/0009-2614(88)80378-6.
[84] M.A. Hamon, K.L. Stensaas, M.A. Sugar, K.C. Tumminello, A.K. Allred, Reacting soluble single-walled carbon nanotubes with singlet oxygen, Chem. Phys. Lett. 447 (2007) 1–4, https://doi.org/10.1016/j.cplett.2007.08.079.
[85] D.R. Kearns, Physical and chemical properties of singlet molecular oxygen, Chem. Rev. 71 (1971) 395–427, https://doi.org/10.1021/cr60272a004.
[86] S. Sarkar, B. Bandyopadhyay, Singlet ($^1\Delta g$) $O_2$ as an efficient tropospheric oxidizing agent: the gas phase reaction with the simplest Criegee intermediate, Phys. Chem. Chem. Phys. 22 (2020) 19870–19876, https://doi.org/10.1039/D0CP02617D.
[87] G.S. Hammond, A correlation of reaction rates, J. Am. Chem. Soc. 77 (1955) 334–338, https://doi.org/10.1021/ja01607a027.